Electronic Supplementary Information for:

Avidity and surface mobility in multivalent ligand-receptor binding

Simon Merminod,[1,*] John R. Edison,[2,†] Huang Fang,[1]
Michael F. Hagan,[1] and W. Benjamin Rogers[1,‡]

[1]*Martin A. Fisher School of Physics,*
Brandeis University, Waltham, MA 02453, USA

[2]*Brandeis Materials Research Science and Engineering Center,*
Brandeis University, Waltham, MA 02453, USA

[*] Current address: Department of Molecular and Cellular Biology, Harvard University, Cambridge, MA 02138, USA

[†] Current address: Department of Chemical and Biomolecular Engineering, Johns Hopkins University, Baltimore, MD 21218, USA

[‡] wrogers@brandeis.edu

CONTENTS

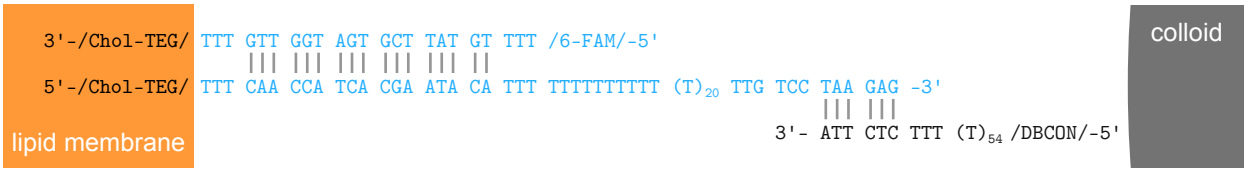

FIG. 1. Schematic of the oligonucleotide sequences of the receptors (left) and the ligands (right). The short vertical grey lines show Watson-Crick base pairing between complementary oligonucleotides.

I. DNA CONSTRUCTS

Transient interactions between a colloidal particle and a supported phospholipid bilayer are due to hybridization of DNA "ligands" and "receptors." We call the DNA molecules grafted to colloids "ligands" and the molecules attached to the lipid bilayer "receptors." The ligands are 63-bases-long, single-stranded, and consist of an inert poly-T spacer and a sticky end on the 3' end (Figure 1). The 5' end is attached to the surface of colloidal particles, as described below (Section II). The sticky end is 6-bases-long and binds the ligand to a receptor. The specific sequences are shown in Figure 1.

The membrane-anchored DNA receptors are complexes formed of two DNA molecules. The short strand is 23-bases-long and has a 6-FAM fluorophore on the 5' end, a TTT spacer, a 17-nucleotides (nt) binding domain, another TTT spacer, and a cholesterol-triethylene glycol (TEG) modification on the 3' end. The long strand is 65-bases-long and consists of a cholesterol-TEG modification on the 5' end, a TTT spacer, a 17-nt binding domain, a 39-bases-long spacer mostly composed of poly-T, and a 6-nt sticky end on the 3' end. The two 17-nt binding domains are complementary to one another. Thus the two receptor molecules hybridize to form the complex shown in Figure 1. The two cholesterol-TEG modifications ensure that the receptors remain bound to the lipid bilayer throughout the duration of our experiment [1]. The fluorophore 6-FAM confirms that the DNA receptors are mobile within the supported bilayer via fluorescence recovery after photobleaching (FRAP).

All three strands are purchased from Integrated DNA Technologies and purified by high-performance liquid chromatography.

II. TPM PARTICLE SYNTHESIS AND LIGAND GRAFTING

We synthesize DNA-grafted colloidal particles made from 3-(trimethoxysilyl)propyl methacrylate (TPM). In brief, we follow a modified version of the method developed by Pine and coworkers [2], which is comprised of three parts: (1) TPM emulsion droplets are polymerized with surface-bound chlorine groups; (2) Chlorine groups on the surface of the TPM particles are substituted with azide groups; and (3) Single-stranded DNA molecules are conjugated to the surface of TPM particles by strain-promoted click chemistry. The specific protocol that we use is described below. Note that sodium azide and ammonium hydroxide are hazardous substances which require specific precautions.

We make chlorine-modified particles by copolymerizing TPM emulsion droplets with 3-chloropropyltrimethoxysilane in five steps. (1) To make TPM emulsion droplets, we add 300 µl of TPM into a 20 ml aqueous solution containing 1% (w/w) ammonium hydroxide and stir for 4 hours at 1000 RPM. (2) We add 30 µl of 3-chloropropyltrimethoxysilane and stir for 30 min. (3) We add 5 ml of 5% (w/w) sodium dodecyl sulfate solution, stir for 10 min, add 7.5 mg of azobis(isobutyronitrile), which initiates polymerization, and stir for 20 min. Then we transfer the solution into an oven at 80 °C for over 4 hours. (4) After polymerization, we wash the TPM particles with a solution containing 0.2% (w/w) Pluronic F-127 four times and resuspend the particles in 10 ml of 0.4% Pluronic F-127 after the final wash.

We substitute the chlorine groups with azide groups to make azide-modified TPM particles. First, we add 10 mg of potassium iodide and 10 ml of 5% sodium azide solution into the particle solution. Then we place the mixture in an oven at 70 °C for 12 hours. After the reaction, we wash the particles with 0.1% (w/w) aqueous Triton X-100 solution and resuspend the particles in 20 ml of 0.1% (w/w) aqueous Triton X-100 solution for storage after the final wash.

Finally, we attach DNA molecules to the azide-modified TPM particles using strain-promoted click chemistry. We mix 317 µl of deionized water, 43 µl of azide-modified TPM particle solution, 20 µl of 100 µM DBCO-modified single-stranded DNA, 40 µl 10x PBS buffer, and place the suspension on a rotator for 24 hours. After the reaction, we wash the DNA-coated particles with 1xTE buffer containing 1% (w/w) Pluronic F-127 five times by centrifugation and resuspension. Then we wash again the particles, with 1xTE five times by centrifugation and resuspension. We store the particles in 1xTE at 4 °C.

III. SAMPLE PREPARATION

We make supported phospholipid bilayers (SLBs) by fusing small unilamellar vesicles (SUVs) on a glass coverslip. Then we functionalize the SLB with DNA receptors by incubation, followed by washing.

The SLBs are made of a mixture of phospholopids. This mixture is composed of 97.1% (w/w) 1,2-dioleoyl-sn-glycero-3-phosphocholine (18:1 DOPC, Avanti Polar Lipids), 2.4% (w/w) 1,2-dioleoyl-sn-glycero-3-phosphoethanolamine-N-[methoxy(poly-ethylene glycol)-2000] (ammonium salt) (18:1 PEG2000 PE, Avanti Polar Lipids), and 0.5% (w/w) Texas Red 1,2-dihexadecanoyl-sn-glycero-3-phosphoethanolamine, triethylammonium salt (Texas Red DHPE, Thermo Fisher Scientific). All lipids are suspended in chloroform and stored in chloroform at −20 °C. Note that chloroform is a hazardous substance which requires specific precautions. PEGylated lipids separate the SLB from the glass coverslip to promote the mobility of membrane-bound objects within the membrane, and to help prevent non-specific binding between colloidal particles and the glass. Texas Red-labeled lipids are used to confirm that the lipids are mobile within the SLB via fluorescence recovery after photobleaching (FRAP).

First, we make an aqueous solution of small unilamellar vesicles. We mix together 1.03 mg of chloroform-suspended lipids in a culture tube at the (w/w) ratios mentioned above. Then we slowly evaporate chloroform to spread the lipids into a dry, thin film at the bottom of the tube. We vacuum desiccate the lipid film for 4 hours to evaporate any remaining chloroform. We hydrate the dried lipid film overnight with 500 µl of 20% glycerol/1xTE hydration buffer to obtain a suspension of large, multilamellar vesicles. The next day, we sonicate the vesicles for 90 minutes to break the multilamellar vesicles into small unilamellar vesicles. Since large vesicles scatter visible light while SUVs do not, we visually inspect the suspension after sonication to make sure that it appears clear. We further dilute the obtained SUV suspension with another 500 µl of hydration buffer to reach a lipid concentration of 1.03 mg/ml in 20% glycerol/1xTE. Finally, we remove any remaining large vesicles by three cycles of centrifugation and dilution. We store the SUV suspension at 4 °C. The final concentration of lipids is 1.03 mg/ml in 20% glycerol/1xTE hydration buffer. We wash all glassware using acetone, ethanol 70%, and ultrapure water. Then we blow the glassware dry with nitrogen and treat it with air plasma.

We make supported lipid bilayers by fusion of SUVs on cleaned glass coverslips. First, we make a custom-made sample chamber using a large glass coverslip and a small glass coverslip, a Parafilm

mask as a spacer, and two PDMS blocks as inlets and outlets. The glass coverslips are washed using acetone, ethanol 70%, and ultrapure water, blown dry with nitrogen, and plama-cleaned. The Parafilm mask is adhered to glass by placing the "sandwich" of glass-Parafilm-glass on a hot plate at 80 °C for roughly 1 minute. The PDMS blocks are designed with a channel at their base, perforated using a hole puncher to create the inlet and outlet, and plasma-bound to the glass coverslip on each side of the Parafilm-glass chamber. Next we seal all interstices with UV-curable optical glue. We fill the sample chamber with SUV suspension diluted to roughly 0.75 mg/ml in 30 mM NaCl/20% glycerol/1xTE and place it on a hot plate at 37 °C for 30 minutes. During this step, the SUVs fuse with the glass substrate to create a supported lipid bilayer. Finally, we wash out excess SUVs using 1 ml of 20% glycerol/1xTE hydration buffer. The buffer is then replaced by washing the chamber a second time with 1 ml of 500 mM NaCl/1xTE.

We functionalize the SLB with DNA receptors by incubation. First, we anneal the DNA receptors by cooling an equimolar solution containing both DNA molecules at concentrations between 5–45 μM in 500 mM NaCl/1xTE from 90 °C to 25 °C at −0.2 °C/min. Next we incubate the SLB with a solution of these FAM-labeled DNA receptors at a concentration between 1–5 μM in 500 mM NaCl/1xTE for 10–60 minutes (Table I). During incubation, pairs of cholesterol molecules incorporate into the SLB [3]. Then we remove any excess receptors by washing with 500 μl of 500 mM NaCl/1xTE. We evaluate the receptor density using confocal fluorescence microscopy and assess their mobility within the SLB using FRAP (TCS SP8, Leica Microsystems GmbH).

Finally, we add DNA-grafted particles at roughly 0.0015% (v/v) in 500 mM NaCl/1xTE and then seal the chamber.

TABLE I. Conditions for functionalization of supported lipid bilayers with DNA receptors.

Relative receptor density	Receptor suspension concentration (μM)	Incubation time (min)	Best-fit density from the model, ρ (μm^{-2})
low	1	10	138
medium	2.5	10	225
high	5	60	250

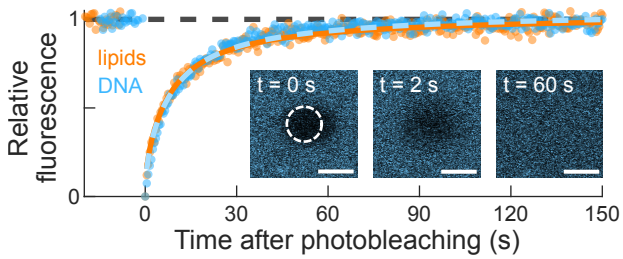

FIG. 2. Relative fluorescence intensity as a function of time after photobleaching for the lipids (orange) and the DNA receptors (blue). Circles are experimental data; solid and dashed curves are model fits using Eq. 3; the horizontal dashed line shows the pre-bleaching fluorescence level. Insets show confocal micrographs of fluorescent DNA receptors after a laser pulse inside the dashed circle. Scalebars, 10 μm.

IV. FLUORESCENCE RECOVERY AFTER PHOTOBLEACHING

We perform fluorescence recovery after photobleaching experiments to estimate the diffusion coefficients of lipids and membrane-bound DNA receptors within the SLBs. We bleach a 10-μm-diameter spot at the center of a roughly 73 μm × 73 μm frame. The reference region is either: (i) a 10-μm-wide square boundary around the edge of the image; or (ii) a 5-μm-wide octagon surrounding the bleached spot with a 10-μm separation. Pre-bleaching consists of 30 frames at a 500 ms time interval. Photobleaching consists of exposing a species to 100% of the available laser power during a short duration. To achieve strong enough photobleaching, we expose the lipids for 7440 ms (or 40 frames); to bleach the DNA receptors we expose for only 372 ms (1 frame). Post-bleaching consists of 500 frames at a 500 ms time interval. All measurements are carried out at room temperature between 21–23 °C. Figure 2 shows examples of FRAP experiments on lipids and DNA receptors within the same membrane.

We normalize all FRAP curves to account for photobleaching and intensity fluctuations in the imaging laser. Specifically, we compute the normalized fluorescence intensity, $I_{\mathrm{dn}}(t)$, using

$$I_{\mathrm{dn}}(t) = \frac{I_{\mathrm{spot}}(t)}{\langle I_{\mathrm{spot}}\rangle_{\mathrm{pre}}} \frac{\langle I_{\mathrm{ref}}\rangle_{\mathrm{pre}}}{I_{\mathrm{ref}}(t)}, \tag{1}$$

where t is the post-bleaching time, $I_{\mathrm{spot}}(t)$ is the intensity of the bleached spot at time t, $\langle I_{\mathrm{spot}}\rangle_{\mathrm{pre}}$ is the average intensity of the bleached spot during the pre-bleaching time, $I_{\mathrm{ref}}(t)$ is the intensity of the reference area at time t, and $\langle I_{\mathrm{ref}}\rangle_{\mathrm{pre}}$ is the average intensity of the reference area during

pre-bleaching time. Then we compute the fluorescence trace, $I_{\mathrm{fluo}}(t)$, according to

$$I_{\mathrm{fluo}}(t) = \frac{I_{\mathrm{dn}}(t) - I_{\mathrm{dn}}(t=0)}{1 - I_{\mathrm{dn}}(t=0)}. \tag{2}$$

We model the FRAP curves assuming a uniform circular beam and full recovery. More specifically, we fit the fractional fluorescence recovery $f(t)$ to the functional form

$$f(t) = \exp\left(-\frac{2\tau}{t}\right)\left[I_0\left(\frac{2\tau}{t}\right) + I_1\left(\frac{2\tau}{t}\right)\right], \tag{3}$$

where I_0 and I_1 are modified Bessel functions of first kind at order 0 and 1, respectively, and τ is the characteristic diffusion time [4]. This functional form is used in Figure 2 to fit the fluorescence recovery of the lipids and the DNA receptors. The diffusion time τ is related to the diffusion coefficient of the fluorophores, D_{f}, and the radius of the circular beam, w_{b}, by

$$\tau = \frac{w_{\mathrm{b}}^2}{4D_{\mathrm{f}}}. \tag{4}$$

In our FRAP experiments, $w_{\mathrm{b}} = 5$ μm and D_{f} ranges between 0.8–1.7 μm^2 s^{-1} (Table II).

We use a laser scanning confocal microscope (TCS SP8, Leica Microsystems GmbH) equipped with a 20x objective (non-immersion, HCX PL Fluotar, numerical aperture, NA = 0.50, Leica Microsystems GmbH) and photomultiplier tubes. We image and carry out FRAP on the Texas Red-labeled lipids with a laser of wavelength 552 nm and on the FAM-labeled receptors with a laser of wavelength 488 nm.

TABLE II. Diffusion coefficients for lipids and DNA receptors at the three receptor densities of the article.

Relative receptor density	D_{lipids} (μm^2 s^{-1})	$D_{\mathrm{receptors}}$ (μm^2 s^{-1})	Best-fit density from the model, ρ (μm^{-2})
low	0.8	1.7	138
medium	1.1	1.2	225
high	1.1	0.9	250

V. OPTICAL SETUP

We use a prism-based, total internal reflection microscope to measure the three-dimensional motion of colloidal particles in the vicinity of a supported lipid bilayer. A 671-nm-wavelength

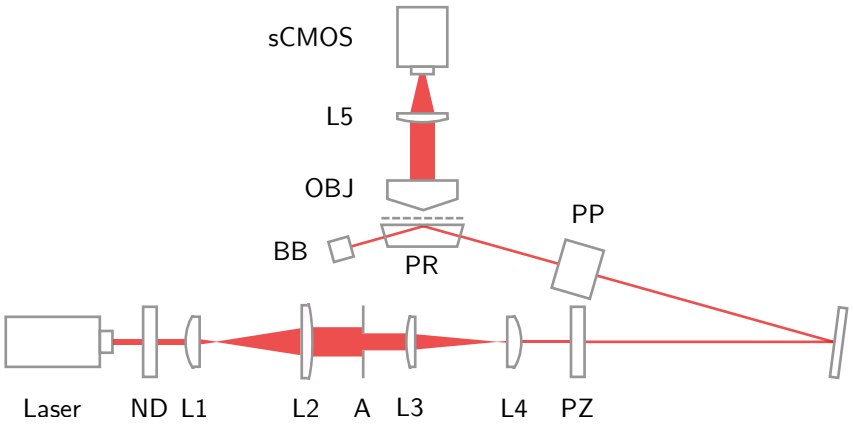

FIG. 3. Optical train of the prism-based total internal reflection microscope. The neutral density filter (ND) adjusts light intensity to prevent saturation in the recorded images while maximizing duration of exposure. The inverted Keplerian telescope made of a pair of spherical, plano-convex lenses (L1 and L2) magnifies the laser beam roughly 8.3x to overfill a 20-mm aperture (A) so as to keep the central part of the Gaussian beam only. The Keplerian telescope made of a pair of spherical, plano-convex lenses (L3 and L4) shrinks the laser beam 10x. The polarizer (PZ) p-polarizes the laser beam before it enters the prism pair (PP) which transforms the beam from circular to elliptical. The elliptical laser beam enters the dove prism (PR) at a right angle and encounters the glass-aqueous sample interface at a 68° angle, where it roughly spreads into a disk. The laser beam generates an evanescent wave inside the sample (dashed line) and is reflected out of the prism into a beam block (BB). The upright microscope composed of an infinity-corrected, 40x objective (OBJ), a spherical, plano-convex lens (L5), and a high-speed sCMOS camera (sCMOS), images the light scattered by colloidal particles from inside the sample.

laser beam (300 mW, SDL-671-LN-300T, Shanghai Dream Lasers) is totally internally reflected at the glass-water interface to create an evanescent wave (Figure 3). Light scattered by colloids diffusing in the evanescent wave is imaged using an upright microscope, consisting of a infinity-corrected 40x objective (Plan Fluor, numerical aperture, NA = 0.75, Nikon Corp.), a tube lens (f_5 = 200 mm, spherical, plano-convex lens, ThorLabs) and a high-speed sCMOS camera (Zyla 5.5, Andor, Oxford Instruments) placed in the image plane of the tube lens. We control the temperature of the sample using a thermoelectric module (TE Technology, Inc.) attached to the prism and a thermistor (TE Technology, Inc.) placed on the sample. The thermoelectric module is cooled by a custom-made water-cooling block.

We shape the imaging laser upstream from the total internal reflection microscope to create a

roughly uniform intensity across the field of view. We first magnify the original beam using a 8.3x inverted Keplerian telescope (f_1 = 60 mm, f_2 = 500 mm, spherical, plano-convex lenses, ThorLabs), of which we crop the outer part of the beam using a 20-mm aperture (ThorLabs). The circular beam is then reduced by a 10x Keplerian telescope (f_3 = 500 mm, f_4 = 50 mm, spherical, plano-convex lenses, ThorLabs), before being p-polarized by a linear polarizer (Thorlabs). We next transform the circular beam into an elliptical beam using an anamorphic prism pair (magnification, 4.0x, Thorlabs) to create a roughly circular spot upon reflection. A Littrow dispersion prism (N-BK7, Edmund Optics) attached on the exit side of a 68-degree dove prism (N-BK7, Tower Optical Corp.) guides the reflected laser beam out of the setup to a beam block. We adjust the beam intensity using a neutral density filter (optical density, OD = 1, Thorlabs). We align the beam using the back reflection from the dove prism-air interface.

VI. CALIBRATION OF THE TOTAL INTERNAL REFLECTION MICROSCOPE

We calibrate the relationship between the scattered intensity and the separation distance using the separation-dependent hydrodynamic interactions between a colloidal particle and a flat wall. We assume that the relationship between the scattered intensity, I, and the separation between the glass substrate and the bottom of the particle, h, is given by

$$I(h) = I_0\, e^{-h/h_0}, \tag{5}$$

where I_0 is the intensity of light scattered by a particle in contact with the glass substrate at $h = 0$ and h_0 is the typical penetration depth of the evanescent wave [5]. Then we determine the parameters I_0 and h_0 using the method from Volpe, Bechinger and co-workers [6], which relies on longstanding hydrodynamic theories of diffusion of a single colloidal particle near a wall [7]. Briefly, we find the parameters I_0 and h_0 that best match the measured distributions of frame-to-frame particle displacements to theoretical predictions over a range of separations between h = 100–300 nm, where there are no DNA interactions. We consider this calibration process to be successful because we obtain a satisfying match between experimental measurements of the transverse component of the diffusion coefficient, $D_{\perp,\mathrm{exp}}(h)$ [8], and theoretical predictions, $D_{\perp,\mathrm{th}}(h)$ [7] (Figure 4).

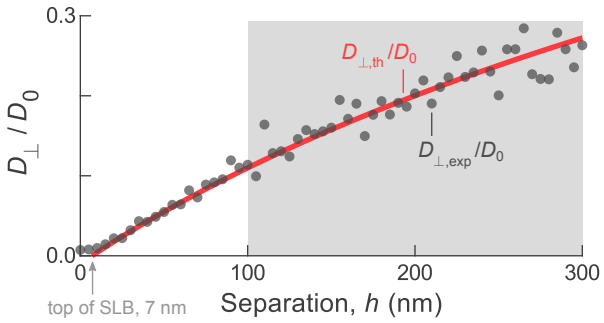

FIG. 4. Example of validation of our calibration routine. Coefficients of transverse diffusion normalized by the Stokes-Einstein coefficient of diffusion, D_0, as a function of particle-glass separation, for an experiment after determining I_0 and h_0. Circles show experimental measurements; the solid red curve shows the theoretical prediction. We assume a non-slip boundary condition at the upper surface of the SLB. We fit I_0 and h_0 within the shaded region, so as to avoid separations at which DNA strands interact.

VII. INTERACTION POTENTIALS

We compute the effective interaction potential between a particle and the supported lipid bilayer at a given temperature by inverting the Boltzmann distribution. Specifically, we compute the histogram of the full separation time-series of a single particle, $P(h)$, and then convert it into a free energy profile, $\Delta F(h)$, by inverting the Boltzmann distribution, $P(h) \propto \exp\left[-\Delta F(h)/k_\mathrm{B}T\right]$, where k_B is the Boltzmann constant and T is the temperature. This free energy contains two main contributions: one from DNA-mediated interactions and another due to gravity. We subtract the gravitational contribution to ΔF to obtain the specific DNA-mediated interaction potentials. For each particle, we take the gravitational potential to be the best fit of a straight line through the interaction potential at separations between 100–300 nm, where we are confident that there are no DNA interactions.

We compare our measured interaction potentials to blurred versions of our theoretical potentials. First, we compute the corresponding distribution of separations for a given model potential using the Boltzmann distribution. Then, to simulate the finite precision of our measurements of the separation, we convolve the distribution with a Gaussian kernel of standard deviation σ_h. This operation smooths the distribution. Then we convert the convolved distribution back into a blurred potential by reinverting the Boltzmann distribution. In practice, this operation makes the potential well shallower and wider than that of the original simulated potential.

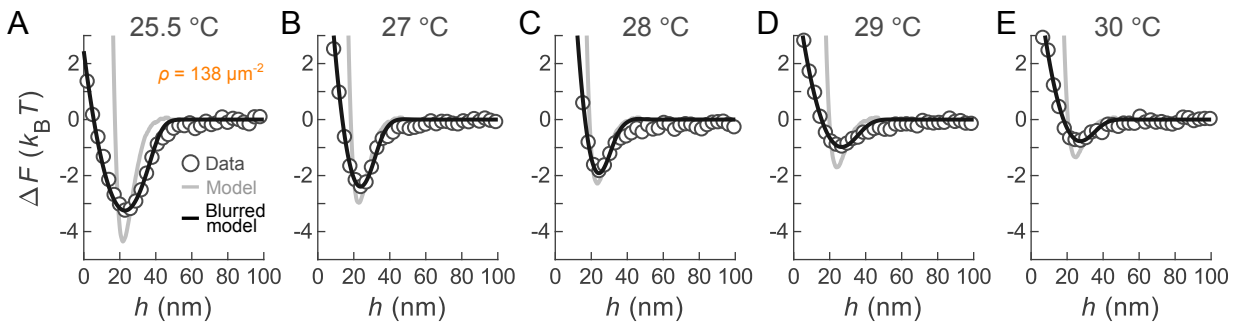

FIG. 5. Colloid-membrane interaction potentials. Interaction potentials from experiments (circles) and numerical simulations (solid curves) for T = 25.5 °C (A), 27 °C (B), 28 °C (C), 29 °C (D), and 30 °C (E), with the receptor density ρ = 138 μm^{-2}. The grey curves show the simulated potentials. The black curves show the corresponding blurred potentials with best-fit temperatures constrained within ±0.25 °C of the measured T, and σ_h = 6.4 nm (A), 3.9 nm (B), 3.0 nm (C), 6.7 nm (D), and 6.0 nm (E). The experimental potentials have been horizontally lined up with the blurred potentials.

Second, we determine the best-fit blurred potentials. We hold the receptor density ρ fixed at the values provided in the main text, and allow the temperature T and our measurement precision σ_h to vary. We take the best-fit blurred potential to be the one that minimizes the sum of squared differences with the experimental potential. We also allow the separation h to freely vary to account for errors in our calibration of I_0 and h_0, with shifts of roughly 0–20 nm. The values that we find for the best-fit temperatures typically vary within ±1.5 °C from the measured temperatures, T, which is due in part to the variability in the binding strength between particles. The values of σ_h vary between 3–9 nm, which is consistent with measurements of particles bound irreversibly to the coverslip.

We find that the blurred potentials match our experimentally measured potentials. Figure 5 shows experimental potentials, theoretical potentials, and the corresponding blurred potentials at selected temperatures for the receptor density ρ = 138 μm^{-2}. The best-fit temperatures are constrained within ±0.25 °C of the measured temperature T. In Figure 5, as well as in Figure 2A–C in the article, experimental potentials were shifted as described above.

VIII. DEFINITION OF THE AVIDITY

We compute the avidity, ΔG_{av}, from the continuous interaction potential, $\Delta F(h)$. Our definition of avidity follows the definition in Ben-Tal *et al.* [9]; it can also be found in Ref. [10]. We define avidity from the integral of the partition function over the *bound state*, which we define as the range of separation distances over which the particle and receptors interact significantly:

$$\Delta G_{\mathrm{av}} = -k_{\mathrm{B}}T \log\left[(c_{\circ}N_{\mathrm{A}})^{1/3}\int_0^{\lambda_{\mathrm{b}}} e^{-\Delta F(h)/k_{\mathrm{B}}T}\mathrm{d}h\right], \tag{6}$$

where $c_{\circ} = 1$ mol/l is a reference concentration, N_{A} is Avogadro's number, and λ_{b} is a binding length scale, or the maximum separation at which ligands can bind to receptors. Since the value of ΔG_{av} changes with λ_{b}, even for separations h at which $\Delta F(h) = 0$, it is important to choose λ_{b} carefully. In our system, we find that $\lambda_{\mathrm{b}} = 34$ nm yields avidities ΔG_{av} that are reasonably insensitive to the precise value of λ_{b}. Thus we set $\lambda_{\mathrm{b}} = 34$ nm for calculations. Note that this measure of avidity—unlike the well-depth of the interaction potential for example—allows one to compare potentials that have different widths or functional forms. Additionally, because we use a Gaussian kernel to obtain the blurred potentials from the theoretical potentials, a given theoretical potential and the blurred potentials obtained from it have the same avidity, whereas the well-depth alone is a strong function of blurring.

With this definition of avidity, even situations with no interaction, $\Delta F(h) = 0$, will contribute to the avidity since there is a non-zero probability of observing such a separation. In contrast, separations with a large free energy $\Delta F(h) \gg 1$, such as small separations where the repulsion dominates, will not contribute to the avidity.

IX. AVIDITY MEASUREMENTS FOR PLOT OF AVIDITY V. TEMPERATURE (FIGURE 2D)

To compute the avidity from the experimental potentials—which are discrete and potentially noisy—we fit them with blurred simulated potentials before evaluating Equation (6). Specifically, for each experimental potential, we find the best-fit blurred potential as described in the previous section, and then compute the avidity from the fitted potential using Equation (6). The obtained avidities constitute the data points in Figure 2D of the article.

Next, for each experimental data set at a given receptor density, we identify the receptor density, ρ, that provides the best fit between theoretical and experimental avidities. Specifically, we compute the avidity as a function of temperature from theoretical potentials for a wide range of ρ. Then we

compare the theoretical avidity at a fixed ρ to the experimental avidity at a fixed receptor density. The best-fit receptor density, ρ, is the one that minimizes the sum of the squared differences between the experimental and theoretical avidities across all temperatures. We find that the experimental data at low receptor density is best fit by simulations at $\rho = 138\ \mu m^{-2}$, the medium receptor density data by $\rho = 225\ \mu m^{-2}$, and the high receptor density data by $\rho = 250\ \mu m^{-2}$.

X. THEORY OF MULTIVALENT LIGAND-RECEPTOR BINDING

We use a recently developed statistical mechanical theory of multivalent interactions to predict the interaction potential between a solid colloid and flat fluid membrane [11]. We begin by discussing the interaction between two flat plates decorated with complementary DNA strands separated by distance h. We then use this information together with the Derjaguin approximation to estimate the interaction between the colloid with fixed tethers and an infinite membrane with mobile tethers. Plate 1 of our system has $N_\mathrm{l} = \rho_\mathrm{l} A$ fixed ligands, where ρ_l is the grafting density of the ligands on the colloid and A is the area of the plate. Plate 2 has mobile receptors and is in contact with a grand canonical reservoir of receptors. When the two surfaces do not interact or when the separation distance $h \to \infty$, the density of receptors equals that of the grand canonical reservoir, which we simply denote ρ. As described by Mognetti, Frenkel and coworkers, [11, 12] we write the adhesion free energy between the two plates as

$$\beta F_\mathrm{adh}(h) = -\log \sum_{N_\mathrm{r}, N_\mathrm{lr}} Z_\mathrm{adh}(h, N_\mathrm{r}, N_\mathrm{lr}), \tag{7}$$

where $Z_\mathrm{adh}(h, N_\mathrm{r}, N_\mathrm{lr})$ gives the weight of microstates that contain N_r receptors and N_lr bonds, and $\beta = 1/k_B T$ is the inverse thermal energy. Note that N_lr is identical to N_b in the article and Section XIV. We assume that the linkers are ideal chains, which allows us to describe $Z_\mathrm{adh}(h, N_\mathrm{r}, N_\mathrm{lr})$ as a product of three terms: $Z^\mathrm{l}_\mathrm{conf}(h, N_\mathrm{l})$, $Z^\mathrm{r}_\mathrm{conf}(h, N_\mathrm{r})$, and $Z_\mathrm{bind}(h, N_\mathrm{r}, N_\mathrm{lr})$. The first two terms correspond to the cost of confining the chains between two plates and the third term gives the likelihood of forming N_lr bonds from N_l ligands and N_r receptors:

$$Z_\mathrm{adh}(h, N_\mathrm{r}, N_\mathrm{lr}) = Z^\mathrm{l}_\mathrm{conf}(h, N_\mathrm{l}) \sum_{N_\mathrm{r}} Z^\mathrm{r}_\mathrm{conf}(h, N_\mathrm{r}) \sum_{N_\mathrm{lr}} Z_\mathrm{bind}(h, N_\mathrm{r}, N_\mathrm{lr}). \tag{8}$$

Using the saddle-point approximation, the sum on the right is approximated to be equal to its dominant term. The dominant term corresponds to $N_\mathrm{lr} = \overline{N_\mathrm{lr}}$ and $N_\mathrm{r} = \overline{N_\mathrm{r}}$, and is found by equating

the first derivative of $Z_{\rm adh}$ with respect to $N_{\rm r}$ and $N_{\rm lr}$ to zero. Note that $\overline{N_{\rm lr}}$ and $\overline{N_{\rm r}}$ are separation h dependent. The adhesion free energy can then be written as

$$\beta F_{\rm adh}(h) = -\log Z^{\rm l}_{\rm conf}(h, N_{\rm l}) - \log Z^{\rm r}_{\rm conf}(h, \overline{N_{\rm r}}) - Z_{\rm bind}(h, \overline{N_{\rm r}}, \overline{N_{\rm lr}}) \tag{9}$$

$$= \beta F^{\rm l}_{\rm conf}(h) + \beta F^{\rm r}_{\rm conf}(h) + \beta F_{\rm bind}(h). \tag{10}$$

The term $F^{\rm l}_{\rm conf}(h) = -k_{\rm B}T \log Z^{\rm l}_{\rm conf}(h)$ is the entropic cost of confining the ligands between two plates separated by distance h,

$$\beta F^{\rm l}_{\rm conf}(h) = -N_{\rm l} \log \chi_l(h), \tag{11}$$

with

$$\chi_{\rm l}(h) = Q_{\rm l}(h)/Q_{\rm l}(\infty), \tag{12}$$

where $Q_{\rm l}(h)$ is the partition function of a ligand tethered at one end and free at the other end confined between two plates separated by distance h. In the next section, we describe how to compute $\chi_{\rm l}(h)$ using Monte-Carlo simulations. In a similar manner for the mobile receptors, $F^{\rm r}_{\rm conf}(h)$ can be written as

$$\beta F^{\rm r}_{\rm conf}(h) = -\overline{N_{\rm r}} \log \chi_{\rm r}(h) - \overline{N_{\rm r}} \log \frac{\rho A}{\overline{N_{\rm r}}} + (\rho A - \overline{N_{\rm r}}). \tag{13}$$

The second term in the above Equation (13) is the chemical potential cost of having $\overline{N_{\rm r}}$ ideal receptors in the system, which is in equilibrium with a grand-canonical reservoir of density ρ.

The partition function $Z_{\rm bind}$ is computed by considering all possible states that have $N_{\rm lr}$ bonds out of $N_{\rm r}$ receptors and $N_{\rm l}$ ligands:

$$Z_{\rm bind}(h, N_{\rm r}, N_{\rm lr}) = \binom{N_{\rm l}}{N_{\rm lr}} \binom{N_{\rm r}}{N_{\rm lr}} N_{\rm lr}!\, \Xi^{N_{\rm lr}}. \tag{14}$$

Each bond has an associated statistical weight Ξ which is proportional to the binding affinity of a ligand-receptor pair and equals $e^{-\Delta G^\circ} \langle e^{-\Delta G_{\rm conf}(h)} \rangle$. Here ΔG° is the temperature-dependent free-energy change associated with hybridization of the complementary base pairs, and $\Delta G_{\rm conf}$ is the confinement-strength-dependent entropic cost associated with connecting the free ends of a ligand and a receptor. Since the receptors are mobile, for a given separation h, we average $\Delta G_{\rm conf}$ over all possible tether positions of the receptor. Therefore we enclose this term in angled brackets.

As mentioned earlier, using the saddle point approximation on Equation (8) we obtain the free energy change associated with ligand-receptor binding as

$$\beta F_{\rm bind}(h) = N_{\rm l} \ln \frac{N_{\rm l} - \overline{N_{\rm lr}}}{N_{\rm l}} + \overline{N_{\rm r}} \ln \frac{\overline{N_{\rm r}} - \overline{N_{\rm lr}}}{\overline{N_{\rm r}}} + \overline{N_{\rm lr}}, \tag{15}$$

where the average number of receptors $\overline{N_{\rm r}}$ and bonds $\overline{N_{\rm lr}}$ are given by

$$\overline{N_{\rm lr}} = \frac{N_{\rm l}\rho A \Xi \chi_{\rm r}}{1 + \rho A \Xi \chi_{\rm r}} \tag{16}$$

$$\overline{N_{\rm r}} = \overline{N_{\rm lr}} + (\rho A \chi_{\rm r}). \tag{17}$$

Putting all the terms together, we obtain

$$\beta F_{\rm adh}(h) = \rho A (1 - \chi_{\rm r}) - N_{\rm l} \log \chi_l - N_{\rm l} \log (1 + \overline{N_{\rm r}} \Xi \chi_{\rm r}). \tag{18}$$

In the next section, we describe our model system specifically and how we use Monte Carlo simulations to compute $\chi_{\rm l/r}$ and Ξ.

XI. MODEL AND NUMERICAL SCHEME

We first compute the interactions between two flat plates separated by a distance h and then use the Derjaguin approximation to estimate the interaction between the colloid and the flat membrane. The lower plate is attached to a grand-canonical reservoir of receptors and the upper plate has ligands anchored at fixed positions. We model the ligands as ideal chains with 10 segments each. The mobile receptors are also ideal chains, and each consists of 8 segments. The length of each segment is given by the Kuhn length of single-stranded DNA, which is 4 nm in 500 mM NaCl [13], as in our experiments. The first segment of the receptor equals 5.8 nm, as it is anchored to the membrane via a short double-stranded DNA domain. All lengths are made dimensionless by the Kuhn length and energies by $k_{\rm B}T$. The interaction between a pair of plates with receptor (reservoir) density ρ and ligand grafting density $\rho_{\rm l}$ is given by Equation (10). Below we describe how we obtain the various terms involved in Equation (18). We employ the simulation techniques suggested in Appendix A of Varilly *et al.* [12]. Details of these simulations can also be found in Reference [14].

Determining the conformational free-energy cost of confining ligands $\beta F^{\rm l}_{\rm conf}(h)$ requires an estimate of $\chi_{\rm l}(h)$, which is the ratio of the partition function of an unbound ligand between two

plates at separation h to the partition function at infinite separation $h \to \infty$, $Q(h)/Q(\infty)$. To obtain this quantity, we use Rosenbluth sampling. In this technique, we grow the chain segment-by-segment. For each segment, we consider k different trial directions chosen from the surface of a sphere with radius equal to the segment length and compute a weight associated with each trial. The weight w_i equals 0 or 1 depending on whether the segment overlaps with the walls or not. We randomly pick one of the k trial segments based on the weight w_i. The overall Rosenbluth weight of the chain is given by $W = \prod_i^{N_{\rm seg}} w_i/k$. Here $N_{\rm seg}$ is the total number of segments in the chain, which equals 8 for the receptors and 10 for the ligands. The average Rosenbluth factor, $\langle W \rangle$, gives $Q(h)/Q_1$, where $Q_1 = \prod_i^{N_{\rm seg}} 4\pi l_i^2$ is the partition function of an ideal chain in bulk and l_i is the segment length. The factor $\chi_{\rm l}(h)$ is obtained from $\langle W \rangle(h)/\langle W \rangle(\infty)$. The conformational cost of confining the receptors $\chi_{\rm r}(h)$, is computed in the same manner.

The attractive part of the interaction between the plates is given by $\beta F_{\rm bind}(h)$. To obtain an estimate of this term, we need to compute $\Xi = e^{-\Delta G^\circ} \langle e^{-\Delta G_{\rm conf}(h)} \rangle$, with $\Delta G^\circ = \Delta H^\circ - T\Delta S^\circ$ as the binding affinity between the sticky ends of the DNA ligands and receptors. For the sequences we use in the experiments $\Delta H^\circ = -40.9$ kcal/mol and $\Delta S^\circ = -0.1184$ kcal/mol K. As mentioned earlier, $\Delta G_{\rm conf}$ is the confinement-strength-dependent entropic cost associated with turning a ligand and a receptor, each initially with one free end, into a single chain that is bound at both ends to the plates. This quantity depends on the distance between the ligand and the receptor $|\mathbf{r}_{\rm l} - \mathbf{r}_{\rm r}|$, and the plate separation h. Since the receptors are mobile, we average this quantity over all possible tether positions of the receptor [15]. For fixed $\{|\mathbf{r}_{\rm l} - \mathbf{r}_{\rm r}|, h\}$ we have

$$\Delta G_{\rm conf}(h) = \frac{p(N_{\rm seg}, |\mathbf{r}_{\rm l} - \mathbf{r}_{\rm r}|)}{\rho_0} \frac{\langle W_{\rm lr} \rangle}{\langle W_{\rm l} \rangle \langle W_{\rm r} \rangle}, \tag{19}$$

where ρ_0 is the standard concentration, $p(N_{\rm seg}, |\mathbf{r}_{\rm l} - \mathbf{r}_{\rm r}|)$ is the probability of having a chain with $N_{\rm seg}$ begin at $|\mathbf{r}_{\rm l}|$ and end at $|\mathbf{r}_{\rm r}|$, or the probability that a chain with $N_{\rm seg}$ has end-to-end distance $|\mathbf{r}_{\rm l} - \mathbf{r}_{\rm r}|$, and $\langle W_{\rm l} \rangle$, $\langle W_{\rm r} \rangle$, and $\langle W_{\rm lr} \rangle$ are defined below. For the case where all the segments are of equal length, exact analytical expressions are available to compute p. Since one of our segments in the receptor is slightly larger than the others, we numerically estimate [16] the probability p from the equation

$$p(N_{\rm seg}, |\mathbf{r}_{\rm l} - \mathbf{r}_{\rm r}|) = \frac{1}{2\pi^2 |\mathbf{r}_{\rm l} - \mathbf{r}_{\rm r}| l_0} \int_0^\infty \frac{\sin(|\mathbf{r}_{\rm l} - \mathbf{r}_{\rm r}| x) \sin(l_0 x) \sin^{N_{\rm seg}-1}(x)}{x^{N_{\rm seg}-1}} {\rm d}x \tag{20}$$

where l_0 is the length of the first segment of the receptors, which in reduced units equals 1.45. $\langle W_{\rm l} \rangle$ and $\langle W_{\rm r} \rangle$ in Equation (19) are average Rosenbluth weights of the unhybridized ligand and

receptor confined between two plates separated by distance h. To obtain the Rosenbluth weight of the hybridized strand $\langle W_{\mathrm{lr}} \rangle$, which is tethered at both ends, we need to modify the Rosenbluth scheme [12]. In the case where the strand is tethered only at one end, we propose the location of new trial segments uniformly on the surface of the sphere. However for the hybridized strand, since both ends are tethered, we need to weigh each trial segment i with the probability to reach the final tether point in $N_{\mathrm{seg}} - i$ steps. This is done using rejection sampling. More details on this scheme can be found in Reference [17].

Once we obtain $\langle \Delta G_{\mathrm{conf}} \rangle$, we can estimate Ξ and use equations (17),(15) and (10) to estimate the interaction between two plates separated by h. This data is used together with the Derjaguin approximation to compute the interaction free-energy between a colloidal particle and the membrane.

The statistical mechanical approach that we describe above assumes that the ligands and receptors are able to equilibrate at each separation between the colloidal particle and the supported membrane. This assumption is reasonable given the relative timescales of colloid motion, receptor diffusion, and DNA hybridization. More specifically, the lowest receptor density in our experiments is $138/\mu\mathrm{m}^2$, thus the receptors are roughly 85 nm apart on average. Assuming a typical receptor diffusion coefficient of $D = 1\ \mu\mathrm{m}^2/\mathrm{s}$ (see Section IV, Table II), we estimate that the time it takes for receptors to move their average spacing is about $(0.085\ \mu\mathrm{m})^2/D = 0.007$ s. In comparison, colloidal particles diffuse in the transverse direction (i.e., vertically) with a diffusion coefficient of roughly $0.01\ \mu\mathrm{m}^2/\mathrm{s}$ when they are near to contact with the SLB. Thus, the typical time for a colloidal particle to leave the vicinity of the membrane surface is about $(45\ \mathrm{nm})^2/(0.01\ \mu\mathrm{m}^2/\mathrm{s}) \approx 0.2$ s. Therefore, it takes roughly 30 times longer for a colloid to leave the neighborhood of the interface where ligands and receptors can interact than for a receptor to diffuse the distance separating it from other receptors. Furthermore, the average bound lifetimes for all but the highest temperatures (and weakest avidities) are even longer than the typical escape time and can be over an order of magnitude longer at the lower temperatures that we explore (Figure 8). As a result, we expect that receptors have time to accumulate within the contact region before the particles unbind and diffuse away. Finally, given that DNA hybridization occurs on timescales that are much faster than the diffusion of micrometer-sized colloidal particles, we expect that the DNA molecules can also relax into their equilibrium distribution. Indeed, equilibrium statistical mechanics has been used successfully to describe the effective interactions that emerge between DNA-coated particles [18, 19].

XII. RECEPTOR RECRUITMENT

Due to their mobility within the fluid lipid bilayer, receptors can be recruited in the gap between a particle and the membrane to form an aggregate. Figure 6A shows the excess number of receptors in the gap as a function of the temperature and separation distance for a fixed receptor density, $\rho = 138\ \mu\text{m}^{-2}$. Note that this figure uses similar data to Figure 3A in the article, but shows the dependence on separation distance instead of using a Boltzmann-averaged value, which Figure 3*A* did. As in the article, the data shows that mobile receptors are always recruited on average, and that recruitment is larger at lower temperatures. Additionally, here we observe that receptor recruitment is a nonmonotonic function of the colloid-membrane separation. More specifically, we find a temperature-dependent separation distance at which receptor recruitment is maximal. Qualitatively, this optimum separates the separation distances at which the entropy loss due to vertical confinement is weak compared to the enthalpy gain due to forming new bonds—the large separations—from the separations at which vertical confinement is strong—the small separations. For a more detailed physical picture on the effect of vertical confinement on receptor recruitment, let us now examine the receptor density profiles.

To strike a balance between the enthalpy gain and the entropy loss, the receptors self-organize at the binding site. Figure 6B shows radial density profiles of mobile receptors relative to the density of their grand canonical reservoir, $\rho = 138\ \mu\text{m}^{-2}$, for selected separations at a fixed temperature $T = 28\ ^\circ\text{C}$. The spatial distribution of mobile receptors is nonuniform, in sharp contrast with the fixed receptors, which are uniformly distributed on the membrane. Furthermore, the shape of the mobile receptor distribution varies with colloid-membrane separation and reveals that receptors self-organize to minimize their entropic cost of confinement while being recruited. At large separations, the highest receptor density occurs at the center of the recruited aggregate. In contrast, at small separations, the receptors accumulate at the periphery of the binding site to maximize their conformational entropy while still binding to ligands. Both of these features are roughly independent of the receptor density ρ.

XIII. WRAPPING OF AN ADHERING PARTICLE BY THE LIPID MEMBRANE

Lipid membranes can undergo elastic deformations. In particular, a membrane can wrap around an adhering particle, either partially or totally. Deserno [20] theoretically predicted the regions

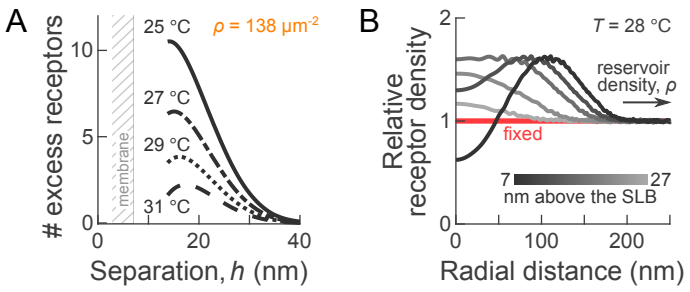

FIG. 6. Receptor recruitment. (A) Model predictions of the excess number of receptors in the gap between the particle and the supported bilayer at selected temperatures for a fixed receptor density $\rho = 138\ \mu\text{m}^{-2}$, showing that receptors are recruited into an aggregate upon binding. (B) Radial density profiles of the receptors relative to the density of the grand canonical reservoir, $\rho = 138\ \mu\text{m}^{-2}$, for different separations: 7–27 nm (black to light gray). The receptors organize at the periphery of the binding site at small separations. The red line shows the uniform density profile for fixed receptors.

of the relevant parameter space where such wrapping occurs, and by what amount. The relevant parameters are the membrane bending rigidity, κ, the membrane tension, σ, the adhering particle radius, a, and the particle-membrane adhesion energy per unit area, w. Deserno defines two dimensionless ratios: $\tilde{w} = 2wa^2/\kappa$ and $\tilde{\sigma} = \sigma a^2/\kappa$. He predicts no membrane deformation for $\tilde{w} < 4$, partial wrapping for $4 < \tilde{w} < 4 + 2\tilde{\sigma}$, and full wrapping for $\tilde{w} > 4 + 2\tilde{\sigma}$. For our DOPC membranes, typical values are $\sigma = 1\ \text{pN nm}^{-1}$ and $\kappa = 20\ k_\text{B}T$ [21, 22]. We take the well-depth of the plate-plate interaction free-energy per unit area computed in the simulations as the adhesion energy, w. We find that w ranges between 30–240 $k_\text{B}T/\mu\text{m}^2$ for ρ between 138–250 μm^{-2} and temperatures between 25–32 °C. Therefore, the dimensionless ratio $\tilde{w}$ ranges between roughly 2–12 and $\tilde{\sigma} \approx 6000$.

We find that wrapping occurs when the avidity is below $-4.7\ k_\text{B}T$. Figure 7 shows $\tilde{w}$ as a function of the avidity from our simulations at the three receptor densities $\rho = 138\ \mu\text{m}^{-2}$, 225 μm^{-2}, and 250 μm^{-2}, and temperatures between 25–32 °C. All of the data collapses on a single curve, for which the condition $\tilde{w} > 4$ corresponds to avidities $\Delta G_\text{av} < -4.7\ k_\text{B}T$.

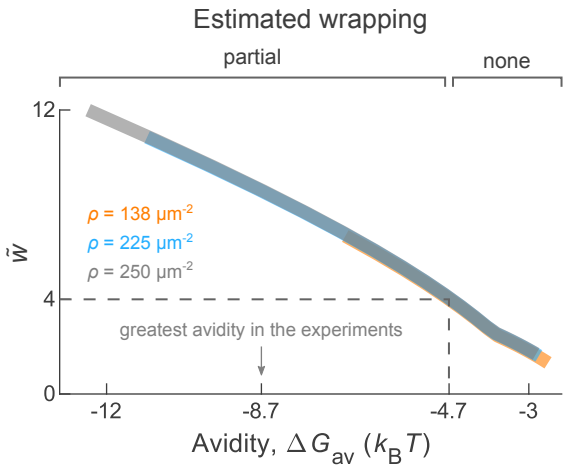

FIG. 7. Estimated wrapping of a colloid adhering to an elastic lipid membrane. The values of dimensionless parameter $\tilde{w}$ tell us whether the membrane is deformed and is computed here for the receptor densities and range of temperature explored in the experiments: $\rho = 138$ μm^{-2}, 225 μm^{-2} and 250 μm^{-2}, and $T = 25$–32 °C. The membrane is predicted to not deform when $\tilde{w} < 4$ and to partially wrap the particle when $\tilde{w} > 4$.

XIV. MOBILITY OF A MEMBRANE-BOUND PARTICLE

A. Identifying the bound state

We determine whether or not a particle is bound based on a separation threshold, h_b. For each particle, we determine h_b from the blurred potential $\beta\Delta F$ that has the same well-depth as the measured potential. Specifically, we take h_b to be the separation distance at which $\beta\Delta F(h_b) = -0.1$. We define h_b as a threshold between the bound state and the unbound state. Next, we define bound events as segments of trajectories for which the separation $h(t)$ is below the threshold h_b. All separations above h_b are considered to be unbound.

B. Bound lifetimes statistics

We define a bound event as an uninterrupted segment of a trajectory during which the particle is always bound. For each of these segments, we measure the lifetime of the bound event. Figure 8 shows the distribution of these bound lifetimes for three different temperatures. For each temperature, we see a broad distribution of lifetimes. The means of the distributions depend on

temperature: The particles stay bound for a longer duration on average at low temperatures as compared to high temperatures. This observation agrees with expectations, since we expect the average bound lifetimes to increase with increasing adhesion strength.

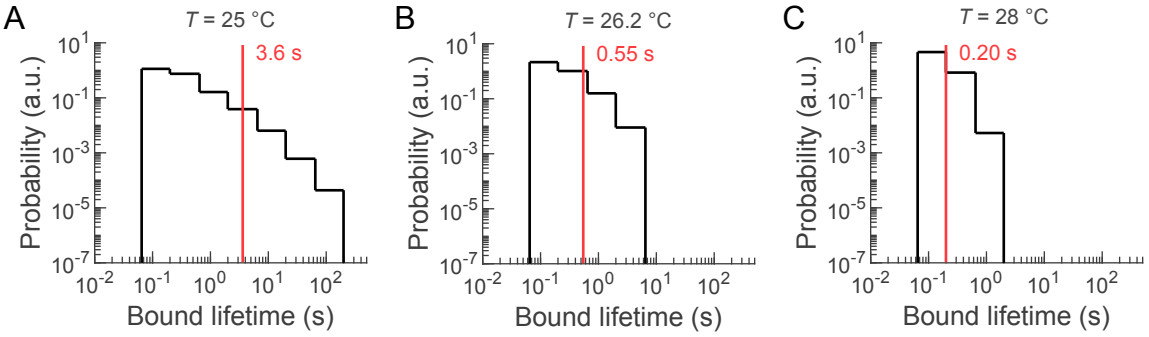

FIG. 8. Bound lifetime distributions at (A) $T = 25$ °C, (B) $T = 26.2$ °C, and (C) $T = 28$ °C for the lowest receptor density, $\rho = 138$ μm^{-2}. The vertical red lines indicate the mean value of each distribution. The ranges of h_b are 41–48 nm (A), 42–45 nm (B), and 38–45 nm (C).

C. Relationships between potential well depth, receptor aggregate properties and avidity

We compute phenomenological relationships between the average number of bonds, $\langle N_\mathrm{b}\rangle$, and the average receptor aggregate radius, R, from our model predictions of the interaction potential $\Delta F(h)$. Specifically, we compute $\langle N_\mathrm{b}\rangle$ as the Boltzmann-average over the number of bonds formed at each separation, $N_\mathrm{b}(h)$:

$$\langle N_\mathrm{b}\rangle = \frac{\int_0^\infty N_\mathrm{b}(h)\, e^{-\beta\Delta F(h)}\mathrm{d}h}{\int_0^\infty e^{-\beta\Delta F(h)}\mathrm{d}h}. \tag{21}$$

Similarly, we compute the Boltzmann-averaged receptor density profiles, $\langle\rho_\mathrm{prof}\rangle(r)$:

$$\langle\rho_\mathrm{prof}\rangle(r) = \frac{\int_0^\infty \rho_\mathrm{prof}(r,h)\, e^{-\beta\Delta F(h)}\mathrm{d}h}{\int_0^\infty e^{-\beta\Delta F(h)}\mathrm{d}h}, \tag{22}$$

where $\rho_\mathrm{prof}(r,h)$ is the receptor density profile at separation h. Finally, we compute normalized receptor profiles $\rho_\mathrm{scaled}(r)$:

$$\rho_\mathrm{scaled}(r) = 2\,\frac{\langle\rho_\mathrm{prof}\rangle(r)/\langle\rho_\mathrm{prof}\rangle(\infty) - 1}{\max[\langle\rho_\mathrm{prof}\rangle(r)/\langle\rho_\mathrm{prof}\rangle(\infty)] - 1} - 1. \tag{23}$$

From each such rescaled profile, we define the average aggregate radius, R, as the radial coordinate at which the density profile $\rho_\mathrm{scaled}(r)$ reaches half its maximum height (Figure 9). In practice, we

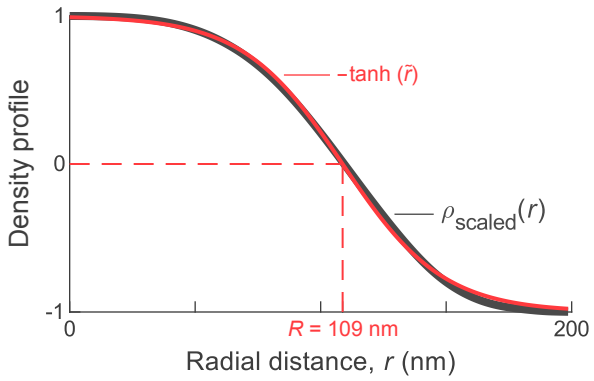

FIG. 9. Estimating the radius of the receptor aggregate from the density profile. Representative rescaled receptor density profile, $\rho_{\mathrm{scaled}}(r)$, as a function of the radial distance to the point of closest contact, r, for receptor reservoir density $\rho = 138\ \mu\mathrm{m}^{-2}$ and $T = 25\ ^{\circ}\mathrm{C}$ (grey curve). The red curve is the best-fit hyperbolic tangent, $-\tanh(\tilde{r})$, with $\tilde{r} = a_{\mathrm{r}} r + b_{\mathrm{r}}$, where a_{r} and b_{r} are adjustable parameters. We define the average aggregate radius, R, as the radial distance at which $\tanh(\tilde{r})$ reaches its half-height. In this example, $R = 109$ nm.

identify the aggregate radius by fitting a hyperbolic tangent of the form $-\tanh(\tilde{r})$, with $\tilde{r} = a_{\mathrm{r}} r + b_{\mathrm{r}}$, where a_{r} and b_{r} are adjustable parameters.

Our model predictions of the average number of bonds per aggregate and the average aggregate radius collapse onto universal curves. Figure 10A,B show $\langle N_{\mathrm{b}} \rangle$ and R as a function of the minimum of the interaction potential, $\min \Delta F$, for the receptor densities and temperature ranges discussed in the article. We find that predictions of $\langle N_{\mathrm{b}} \rangle$ for all three densities collapse onto a single curve (Figure 10A). This curve is similar to earlier models of multivalent binding, which predicted that $\min \Delta F$ is proportional to the average number of bridges [18, 23]. Similarly, predictions of R collapse onto a single curve for all three densities (Figure 10B). Although we do not have closed-form analytic expressions for $\langle N_{\mathrm{b}} \rangle$ or R, we can fit phenomenological expressions to the two curves. Most importantly, these two expressions provide a link between an experimental observable—namely the well depth—and two microscopic parameters—the average number of bridges and the aggregate radius—that we use to test model predictions of the lateral mobility of inclusions within a membrane. In practice, we subtract the average well depth of the nonspecific interaction potentials—roughly $1\ k_{\mathrm{B}}T$—from the well depth of each experimental potential before we use the phenomenological expressions shown in Figure 10A,B to infer values of $\langle N_{\mathrm{b}} \rangle$ and R. Figure 10C shows the roughly linear relationship between the avidity and the well depth.

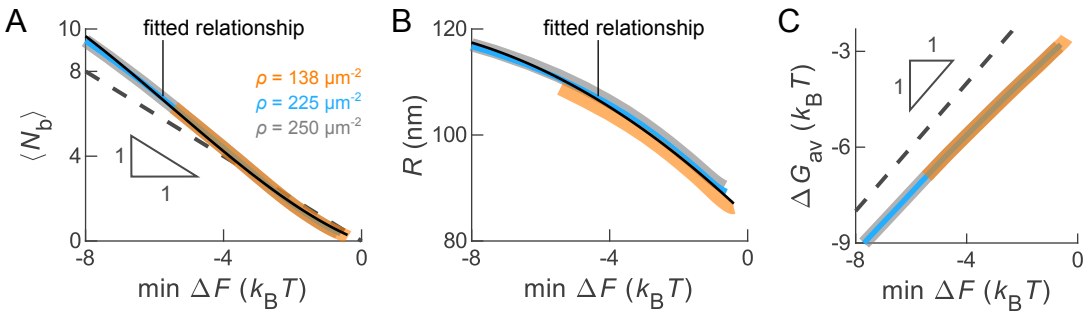

FIG. 10. Relationships between the well depth, the number of bridges, the aggregate radius, and the avidity. The thick colored curves are simulation results for $\rho = 138$ μm^{-2} (orange), 225 μm^{-2} (blue) and 250 μm^{-2} (grey). (A) The average number of bonds is a slightly nonlinear function of the well depth. The dashed line shows $\langle N_\mathrm{b}\rangle = -\min(\Delta F/k_\mathrm{B}T)$. The black solid curve is a fitted polynomial relationship. The average number of bonds behaves similarly to earlier models [18, 23]. (B) The average aggregate radius increases with the well depth. The black solid curve is a fitted polynomial relationship. (C) The avidity is a roughly linear function of the well depth. The dashed line shows $\Delta G_\mathrm{av} = \min \Delta F$.

D. Diffusion of permeable membrane inclusions

Consider an inclusion composed of an aggregate of many identical units diffusing within a lipid membrane. If the lipid molecules in the membrane can freely drain between the units, then the units are *not* coupled to one another hydrodynamically. In this limit, the total drag on the inclusion is just the sum of the drag on the motion of each unit. If the units are identical, the total drag is proportional to the number of units. Combining these assumptions with the Stokes-Einstein relationship, the diffusion coefficient of an inclusion should scale as the inverse of the average number of units: $D_\text{free-draining} \propto \langle N_\mathrm{b}\rangle^{-1}$. This prediction is often referred to as the *free-draining* model [24–27].

E. Diffusion of unit-aggregate inclusions

Now consider a different limit, in which the units composing the inclusion behave as a unit-aggregate that *cannot* be penetrated by lipid molecules within the membrane. In this case, the inclusion can be viewed as a non-permeable cylinder diffusing within the membrane. We denote the cylinder radius by R.

1. In free membranes

Saffman and Delbrück calculated the translational diffusion coefficient of a unit-aggregate inclusion within a free membrane [28]:

$$\beta D_{\mathrm{SD}} = \frac{1}{4\pi\eta_{\mathrm{m}}h_{\mathrm{m}}}\left[\ln\frac{2}{\varepsilon'} - \gamma\right], \tag{24}$$

where η_{m} is the two-dimensional dynamic viscosity of the membrane, η_{3D} is the bulk dynamic viscosity of the aqueous buffer, h_{m} is the membrane thickness, $\gamma = 0.5772$ is the Euler constant, and

$$\varepsilon' = \frac{R}{h_{\mathrm{m}}}\frac{2\eta_{\mathrm{3D}}}{\eta_{\mathrm{m}}} \tag{25}$$

is a dimensionless inclusion radius. The Saffman-Delbrück model is relevant if $\varepsilon' \leq 0.1$ [29]. In our experiment, $\varepsilon' = 0.23$–0.30, thus we cannot use the Saffman-Delbrück model directly.

Hughes, Pailthorpe and White (HPW) derived a generalization of Equation (24) for arbitrary ε' [29]. To avoid the complicated numerical computations involved, we use the second-order approximation of the HPW results multiplied by the Petrov-Schwille correction [30], which gives an accurate approximation for $\varepsilon' < 10^3$:

$$\beta D_{\text{SDHPW-PS}} = \frac{1}{4\pi\eta_{\mathrm{m}}h_{\mathrm{m}}}\left[\ln\frac{2}{\varepsilon'} - \gamma + \frac{4\varepsilon'}{\pi} - \frac{\varepsilon'^2}{2}\ln\frac{2}{\varepsilon'}\right] \times \left[1 - \frac{\varepsilon'^3}{\pi}\ln\frac{2}{\varepsilon'} + \frac{c_1\varepsilon'^{b_1}}{1 + c_2\varepsilon'^{b_2}}\right]^{-1}, \tag{26}$$

where $c_1 = 0.73761$, $b_1 = 2.74819$, $c_2 = 0.52119$, and $b_2 = 0.61465$.

We find that models describing the diffusion of unit-aggregate inclusions within free membranes do not describe our experimental measurements. Figure 11A shows all of our experimental measurements of the dimensionless diffusion coefficient $D^*_{\text{SDHPW-PS}} = 4\pi\eta_{\mathrm{m}}h_{\mathrm{m}}\beta D_{\text{SDHPW-PS}}$ plotted as a function of the dimensionless aggregate radius ε'. All values of $D^*_{\text{SDHPW-PS}}$ are grouped together, but are roughly one order of magnitude smaller than the model predictions. Thus this model fails to predict the translational mobility of the membrane-bound particles in our experiments. We hypothesize that this disagreement between experiment and theory arises due to hydrodynamic coupling between the receptor aggregate and the glass substrate.

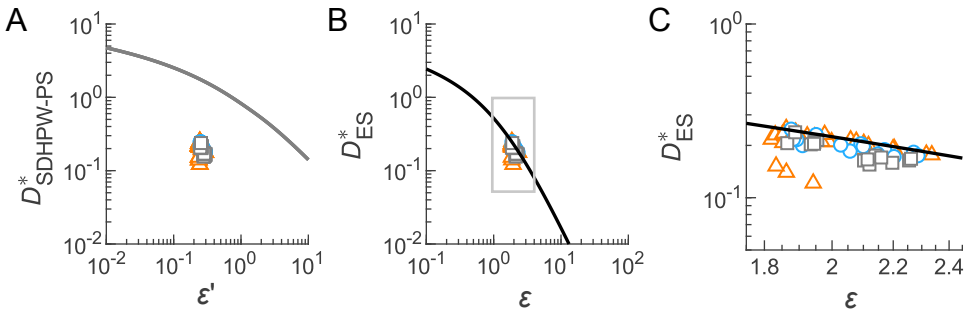

FIG. 11. Mobility of membrane-bound particles. The symbols are all of our experimental measurements. The curves show the models with no adjustable parameters. (A) The model by Hughes, Pailthorpe, White and others [28–30] describing the diffusion of unit-aggregate inclusions in *free* membranes, $D^*_{\mathrm{SDHPW\text{-}PS}}(\varepsilon') = 4\pi\eta_{\mathrm{m}}h_{\mathrm{m}}\beta D_{\mathrm{SDHPW\text{-}PS}}(\varepsilon')$, from Equation (26), fails to predict the experimental measurements. (B) In contrast, a model by Evans and Sackmann [31] predicting the diffusion of unit-aggregate inclusions in *supported* membranes, $D^*_{\mathrm{ES}}(\varepsilon) = 4\pi\eta_{\mathrm{m}}h_{\mathrm{m}}\beta D_{\mathrm{ES}}(\varepsilon)$, from Equation (27), quantitatively describes both the magnitude and the trend of our data. (C) Enlarged boxed region from panel (B), identical to Figure 4D in the article. D^*_{ES} is identical to D^* in the article.

2. *In supported membranes*

Evans and Sackmann calculated the translational diffusion coefficient of a unit-aggregate inclusion within a supported membrane [31]:

$$\beta D_{\mathrm{ES}} = \frac{1}{4\pi\eta_{\mathrm{m}}h_{\mathrm{m}}}\left[\frac{\varepsilon^2}{4}\left(1+\frac{b_{\mathrm{p}}}{b_{\mathrm{s}}}\right)+\frac{\varepsilon K_1(\varepsilon)}{K_0(\varepsilon)}\right], \tag{27}$$

where b_{s} is the membrane-substrate coefficient of friction, b_{p} is the inclusion-substrate coefficient of friction, K_ν is the modified Bessel function of the second kind at order ν, and

$$\varepsilon = R\left(\frac{b_{\mathrm{s}}}{\eta_{\mathrm{m}}h_{\mathrm{m}}}\right)^{1/2} \tag{28}$$

is a dimensionless aggregate radius. This model accounts for the drag on the inclusion due to the substrate, instead of simply the drag on the inclusion due to the membrane, as in the model for free membranes detailed above.

We estimate the parameters in Equation (27) as follows. To start with, we estimate the size of the gap between the lower leaflet of the bilayer membrane and the glass substrate, which we denote H. Indeed if H is small enough, the expression of ε in Equation (28) can be replaced by a more convenient expression independent from b_{s}.

On the membranes that we make, PEG is in the brush regime with a brush thickness of approximately 3.1 nm. Qualitatively, the transition between the mushroom regime and the brush regime for a polymer species grafted on a surface occurs when the grafted density is large enough that it becomes entropically favorable for the polymer molecules to favor extending transversely from the surface. For polymers grafted on lipids of a bilayer, this transition occurs when the fraction of polymer-grafted lipids, X_{poly}, reaches the threshold

$$X_{\mathrm{poly}}^{\mathrm{m}\to\mathrm{b}} = \frac{A_{\mathrm{l}}}{\pi a_{\mathrm{m}}^2} n_{\mathrm{poly}}^{-6/5}, \tag{29}$$

with A_{l} the membrane surface area per lipid molecule, a_{m} the size of a monomer unit, and n_{poly} the degree of polymerization [32]. In our experiments, DOPC lipids have each a surface area $A_{\mathrm{l}} = 0.68$ nm^2 [33], one oxyethylene monomer unit of PEG is of length $a_{\mathrm{m}} = 0.39$ nm [32], and the degree of polymerization of PEG(2k) is $n_{\mathrm{PEG}} = 45$, thus the threshold fraction of PEG is $X_{\mathrm{PEG}}^{\mathrm{m}\to\mathrm{b}} = 0.015$. We can now compare this threshold value with the fraction of PEGylated lipids in our experiments, which is $X_{\mathrm{PEG}} = 0.024$ (see Section III). We find that $X_{\mathrm{PEG}} > X_{\mathrm{PEG}}^{\mathrm{m}\to\mathrm{b}}$, implying that PEG is in the brush regime. With this information, we can estimate the equilibrium length of the PEG chains on our bilayers [32]:

$$L_{\mathrm{PEG}} \approx n_{\mathrm{PEG}}\, a_{\mathrm{m}}^{5/3} \left(\frac{X_{\mathrm{PEG}}}{A_{\mathrm{l}}}\right)^{1/3}, \tag{30}$$

which roughly equals 3.1 nm. Now assuming that this theoretical equilibrium length sets the separation between the PEGylated bilayer and the glass substrate, H, we take $H = 3.1$ nm.

The small value of H makes the lubrication approximation valid and thus enables us to use an approximate expression of ε. The lubrication approximation,

$$b_{\mathrm{s}} \approx \eta_{\mathrm{3D}}/H, \tag{31}$$

is valid when the thickness of the layer between the membrane and the substrate, H, is much smaller than the characteristic length R/ε' [31]. In our experiments, $R/\varepsilon' \approx 340$–$390$ nm, thus $H \ll R/\varepsilon'$. We can therefore use Equation (31) to rewrite ε as

$$\varepsilon \approx \left(\frac{\varepsilon' R}{2H}\right)^{1/2}, \tag{32}$$

which we use in Figure 4D in the article and here in Figure 11B,C.

We use the following values for the other physical constants: η_{m}, the membrane two-dimensional dynamical viscosity, on which the correction due to $< 1\%$ cholesterol is negligible [34], ranges

between 0.14–0.19 Pa s depending on temperature [35]; η_{3D}, the bulk dynamical viscosity of the aqueous buffer with 500 mM NaCl, ranges between 0.80–0.93 mPa s depending on temperature [36]; h_m, the membrane thickness, is 3.8 nm [33, 37]; and we assume $b_s = b_p$.

---

[1] A. Lundgren, B. Agnarsson, R. Zirbs, V. P. Zhdanov, E. Reimhult, and F. Höök, Nonspecific colloidal-type interaction explains size-dependent specific binding of membrane-targeted nanoparticles, ACS Nano **10**, 9974 (2016).

[2] Y. Wang, Y. Wang, X. Zheng, É. Ducrot, J. S. Yodh, M. Weck, and D. J. Pine, Crystallization of DNA-coated colloids, Nat. Commun. **6**, 7253 (2015).

[3] I. Pfeiffer and F. Höök, Bivalent cholesterol-based coupling of oligonucletides to lipid membrane assemblies, J. Am. Chem. Soc. **126**, 10224 (2004).

[4] D. M. Soumpasis, Theoretical analysis of fluorescence photobleaching recovery experiments, Biophys. J. **41**, 95 (1983).

[5] D. C. Prieve, Measurement of colloidal forces with TIRM, Adv. Colloid Interface Sci. **82**, 93 (1999).

[6] G. Volpe, T. Brettschneider, L. Helden, and C. Bechinger, Novel perspectives for the application of total internal reflection microscopy, Opt. Express **17**, 23975 (2009).

[7] H. Brenner, The slow motion of a sphere through a viscous fluid towards a plane surface, Chem. Eng. Sci. **16**, 242 (1961).

[8] J. C. Crocker, Measurement of the hydrodynamic corrections to the brownian motion of two colloidal spheres, J. Chem. Phys. **106**, 2837 (1997).

[9] N. Ben-Tal, B. Honig, C. K. Bagdassarian, and A. Ben-Shaul, Association entropy in adsorption processes, Biophys. J. **79**, 1180 (2000).

[10] M. F. Hagan, A theory for viral capsid assembly around electrostatic cores, J. Chem. Phys. **130**, 114902 (2009).

[11] B. M. Mognetti, P. Cicuta, and L. Di Michele, Programmable interactions with biomimetic DNA linkers at fluid membranes and interfaces, Rep. Prog. Phys. **82**, 116601 (2019).

[12] P. Varilly, S. Angioletti-Uberti, B. M. Mognetti, and D. Frenkel, A general theory of DNA-mediated and other valence-limited colloidal interactions, J. Chem. Phys. **137**, 094108 (2012).

[13] M. C. Murphy, I. Rasnik, W. Cheng, T. M. Lohman, and T. Ha, Probing single-stranded DNA conformational flexibility using fluorescence spectroscopy, Biophys. J. **86**, 2530 (2004).

[14] D. Frenkel and B. Smit, *Understanding Molecular Simulation: From Algorithms to Applications*, Vol. 1 (Academic Press, San Diego, CA, 2001).

[15] S. Angioletti-Uberti, P. Varilly, B. M. Mognetti, and D. Frenkel, Mobile linkers on DNA-coated colloids: Valency without patches, Phys. Rev. Lett. **113**, 128303 (2014).

[16] C.-h. Hsiung, H.-c. Hsiung, and A. A. Gordus, A closed general solution of the probability distribution function for three-dimensional random walk processes, J. Chem. Phys. **34**, 535 (1961).

[17] B. Oyarzún and B. M. Mognetti, Efficient sampling of reversible cross-linking polymers: Self-assembly of single-chain polymeric nanoparticles, J. Chem. Phys. **148**, 114110 (2018).

[18] W. B. Rogers and J. C. Crocker, Direct measurements of DNA-mediated colloidal interactions and their quantitative modeling, Proc. Natl. Acad. Sci. U.S.A. **108**, 15687 (2011).

[19] R. Dreyfus, M. E. Leunissen, R. Sha, A. V. Tkachenko, N. C. Seeman, D. J. Pine, and P. M. Chaikin, Simple quantitative model for the reversible association of DNA coated colloids, Phys. Rev. Lett. **102**, 048301 (2009).

[20] M. Deserno, Elastic deformation of a fluid membrane upon colloid binding, Phys. Rev. E **69**, 031903 (2004).

[21] B. Gumí-Audenis, L. Costa, L. Ferrer-Tasies, I. Ratera, N. Ventosa, F. Sanz, and M. I. Giannotti, Pulling lipid tubes from supported bilayers unveils the underlying substrate contribution to the membrane mechanics, Nanoscale **10**, 14763 (2018).

[22] S. Zuraw-Weston, D. A. Wood, I. K. Torres, Y. Lee, L.-S. Wang, Z. Jiang, G. R. Lázaro, S. Wang, A. A. Rodal, M. F. Hagan, V. M. Rotello, and A. D. Dinsmore, Nanoparticles binding to lipid membranes: From vesicle-based gels to vesicle tubulation and destruction, Nanoscale **11**, 18464 (2019).

[23] P. L. Biancaniello, A. J. Kim, and J. C. Crocker, Colloidal interactions and self-assembly using DNA hybridization, Phys. Rev. Lett. **94**, 058302 (2005).

[24] P. J. Flory, *Principles of Polymer Chemistry* (Cornell University Press, Ithaca, NY, 1953).

[25] D. F. Kucik, E. L. Elson, and M. P. Sheetz, Weak dependence of mobility of membrane protein aggregates on aggregate size supports a viscous model of retardation of diffusion, Biophys. J. **76**, 314 (1999).

[26] J. D. Knight, M. G. Lerner, J. G. Marcano-Velázquez, R. W. Pastor, and J. Falke, Single molecule diffusion of membrane-bound proteins: Window into lipid contacts and bilayer dynamics, Biophys. J. **99**, 2879 (2010).

[27] S. Block, V. P. Zhdanov, and F. Höök, Quantification of multivalent interactions by tracking single

biological nanoparticle mobility on a lipid membrane, Nano Lett. **16**, 4382 (2016).

[28] P. G. Saffman and M. Delbrück, Brownian motion in biological membranes, Proc. Natl. Acad. Sci. U.S.A. **72**, 3111 (1975).

[29] B. D. Hughes, B. A. Pailthorpe, and L. R. White, The translational and rotational drag on a cylinder moving in a membrane, J. Fluid Mech. **110**, 349 (1981).

[30] E. P. Petrov and P. Schwille, Translational diffusion in lipid membranes beyond the Saffman-Delbrück approximation, Biophys. J. **94**, L41 (2008).

[31] E. Evans and E. Sackmann, Translational and rotational drag coefficients for a disk moving in a liquid membrane associated with a rigid substrate, J. Fluid Mech. **194**, 553 (1988).

[32] D. Marsh, R. Bartucci, and L. Sportelli, Lipid membranes with grafted polymers: Physicochemical aspects, Biochim. Biophys. Acta, Biomembr. **1615**, 33 (2003).

[33] A. S. Reddy, D. T. Warshaviak, and M. Chachisvilis, Effect of membrane tension on the physical properties of DOPC lipid bilayer membrane, Biochim. Biophys. Acta, Biomembr. **1818**, 2271 (2012).

[34] A. Filippov, G. Orädd, and G. Lindblom, The effect of cholesterol on the lateral diffusion of phospholipids in oriented bilayers, Biophys. J. **84**, 3079 (2003).

[35] Y. Wu, M. Štefl, A. Olzyńska, M. Hof, G. Yahioglu, P. Yip, D. R. Casey, O. Ces, J. Humpolíčková, and M. K. Kuimova, Molecular rheometry: Direct determination of viscosity in Lo and Ld lipid phases via fluorescence lifetime imaging, Phys. Chem. Chem. Phys. **15**, 14986 (2013).

[36] A. A. Aleksandrov, E. Dzhuraeva, and V. Utenkov, Viscosity of aqueous solutions of sodium chloride, High Temp. **50**, 354 (2012).

[37] B. A. Bergenståhl and P. Stenius, Phase diagrams of dioleoylphosphatidylcholine with formamide, methylformamide and dimethylformamide, J. Phys. Chem. **91**, 5944 (1987).